Airborne Scanning Spectrometer for Remote Sensing of Cloud, Aerosol, Water Vapor, and Surface Properties

MICHAEL D. KING,* W. PAUL MENZEL,† PATRICK S. GRANT,# JEFFREY S. MYERS,# G. THOMAS ARNOLD,@ STEVEN E. PLATNICK,& LIAM E. GUMLEY,** SI-CHEE TSAY,* CHRISTOPHER C. MOELLER,** MICHAEL FITZGERALD,# KENNETH S. BROWN,* AND FRED G. OSTERWISCH††

* *NASA/Goddard Space Flight Center, Greenbelt, Maryland*
† *NOAA/NESDIS, University of Wisconsin—Madison, Madison, Wisconsin*
# *ATAC, NASA/Ames Research Center, Moffett Field, California*
@ *Applied Research Corporation, Goddard Space Flight Center, Greenbelt, Maryland*
& *Research and Data Systems Corporation, Goddard Space Flight Center, Greenbelt, Maryland*
** *Cooperative Institute for Meteorological Satellite Studies, University of Wisconsin—Madison, Madison, Wisconsin*
†† *Dædalus Enterprises, Incorporated, Ann Arbor, Michigan*

(Manuscript received 18 July 1995, in final form 8 December 1995)

ABSTRACT

An airborne scanning spectrometer was developed for measuring reflected solar and emitted thermal radiation in 50 narrowband channels between 0.55 and 14.2 μm. The instrument provides multispectral images of outgoing radiation for purposes of developing and validating algorithms for the remote sensing of cloud, aerosol, water vapor, and surface properties from space. The spectrometer scans a swath width of 37 km, perpendicular to the aircraft flight track, with a 2.5-mrad instantaneous field of view. Images are thereby produced with a spatial resolution of 50 m at nadir from a nominal aircraft altitude of 20 km. Nineteen of the spectral bands correspond closely to comparable bands on the Moderate Resolution Imaging Spectroradiometer (MODIS), a facility instrument being developed for the Earth Observing System to be launched in the late 1990s. This paper describes the optical, mechanical, electrical, and data acquisition system design of the MODIS Airborne Simulator and presents some early results obtained from measurements acquired aboard the National Aeronautics and Space Administration ER-2 aircraft that illustrate the performance and quality of the data produced by this instrument.

1. Introduction

The Moderate Resolution Imaging Spectroradiometer (MODIS) is being developed as part of the Earth Observing System (EOS) to meet the scientific needs for global remote sensing of clouds, aerosols, water vapor, land, and ocean properties from space. MODIS, with 36 spectral channels, is scheduled to be launched in 1998 on the EOS AM-1 platform (King et al. 1995). In support of MODIS remote sensing algorithm development, the MODIS Airborne Simulator (MAS) has been developed by Dædalus Enterprises, Inc., for NASA's high-altitude ER-2 research aircraft, and is an outgrowth of the development of the Wildfire infrared imaging spectrometer, originally designed for investigations of high-temperature terrestrial targets such as forest fires.

With the cooperation of the High Altitude Missions Branch at NASA Ames Research Center, and with input from the MODIS science team, Wildfire was converted to the MAS and continually upgraded over a series of several experiments, starting with the First ISCCP Regional Experiment cirrus campaign (FIRE II) in November 1991. Initial modifications included increasing the dynamic range of the thermal infrared channels to encompass cold cloud targets as well as warm terrestrial surface targets and extending the wavelength response in the visible and infrared regions. Modifications were made as field experiments allowed. In the past several years, upgrades included new detector arrays, grating modifications, an improved broadband lens for the infrared channels, new dewars, and various electronics improvements, all of which resulted in improved in-flight radiometric performance. The overall goal was to modify the spectral coverage and gains of the MAS in order to emulate as many of the MODIS spectral channels as possible.

Since 1991, MAS has flown in many field experiments throughout the world, providing critical datasets for assessing the scientific capability and usefulness of MODIS channels. In addition, with its much higher spatial resolution (50 m vs 250–1000 m for MODIS), MAS is able to provide unique information on the small-scale distribution of various geophysical param-

Corresponding author address: Dr. Michael D. King, NASA/GSFC, Code 900, Greenbelt, MD 20771.

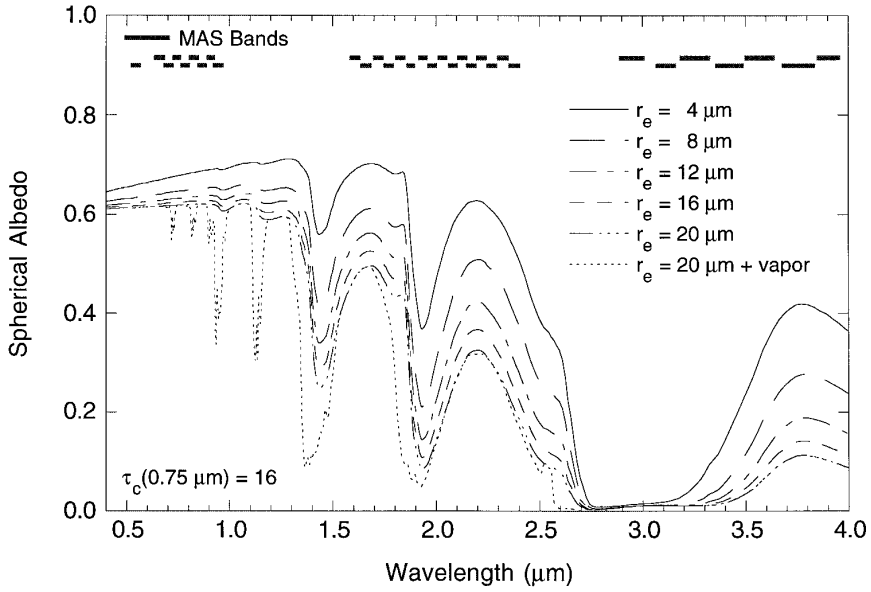

FIG. 1. Cloud spherical albedo as a function of wavelength for selected values of the effective radius of cloud droplets. Results apply to water clouds having a modified gamma distribution with an effective variance $v_e = 0.111$, cloud optical thickness τ_c (0.75 μm) = 16, and saturated water vapor $w_g = 0.45$ g cm^{-2}. The location and bandwidth of MAS channels 1–32 are also shown in the figure.

eters. Initially, MAS used a 12-channel, 8-bit data system that somewhat constrained the full benefit of having a 50-channel scanning spectrometer. Beginning in January 1995, a 50-channel, 16-bit digitizer was used, which greatly enhanced the capability of MAS to simulate MODIS data over a wide range of environmental conditions.

In this paper, we briefly review the spectral characteristics of the earth–atmosphere system from the visible to the infrared and describe the purpose and location of many of the MAS spectral channels. We then describe the optical, mechanical, electrical, and data acquisition system design of the MAS and describe the various methods that have been used to calibrate the spectrometer. Finally, we present selected results obtained from radiometric observations obtained aboard the NASA ER-2 aircraft to demonstrate the performance of the instrument.

2. Spectral applications of MAS

The locations of the MAS spectral channels were chosen to enable a wide variety of earth science applications. Of the 50 MAS channels, 19 have corresponding channels on MODIS. Scientific uses of the MODIS channels have been reviewed by Ardanuy et al. (1991), King et al. (1992), and Running et al. (1994). The remaining MAS channels fill in the spectral region around MODIS locations and some provide unique coverage. In this section we briefly describe the applications for which MODIS and MAS are best suited, based in part on the atmospheric transmittance and reflectance properties of the earth–atmosphere system across the MAS spectral range.

One application of the MAS solar channels is the study of cloud properties at high spatial resolution. Calculations of liquid water cloud reflectance throughout the solar spectrum are shown in Fig. 1 for a wide variety of cloud droplet effective radii (a useful moment of the droplet size distribution) and for the cloud optical thickness (at 0.75 μm) of 16. The MAS channel locations are indicated in the upper portion of this figure. The majority of the molecular absorption in the shortwave region of the solar spectrum is due to water vapor, with some ozone absorption in the broad Chappuis band ($\sim$0.6 μm) continuum. It is clear from this figure that reflectance measurements in the 1.61-, 2.13-, and 3.74-μm windows provide useful information on the cloud droplet size. Reflectance measurements in the visible wavelength region, in contrast, show little variation with droplet size and can thus be used to retrieve cloud optical thickness (cf. Twomey and Cocks 1989; Nakajima and King 1990). The reflectance at 0.94 μm is attenuated by atmospheric water vapor; these measurements, in conjunction with spectrally close atmospheric window reflectances, can provide an estimate of the total precipitable water in cloud-free regions (Kaufman and Gao 1992).

Cloud properties can also be estimated from the thermal bands. Figure 2 shows the top-of-the-atmosphere brightness temperature as a function of wavenumber (wavelength) from 600 to 3340 cm^{-1} (3–16.7 μm) for

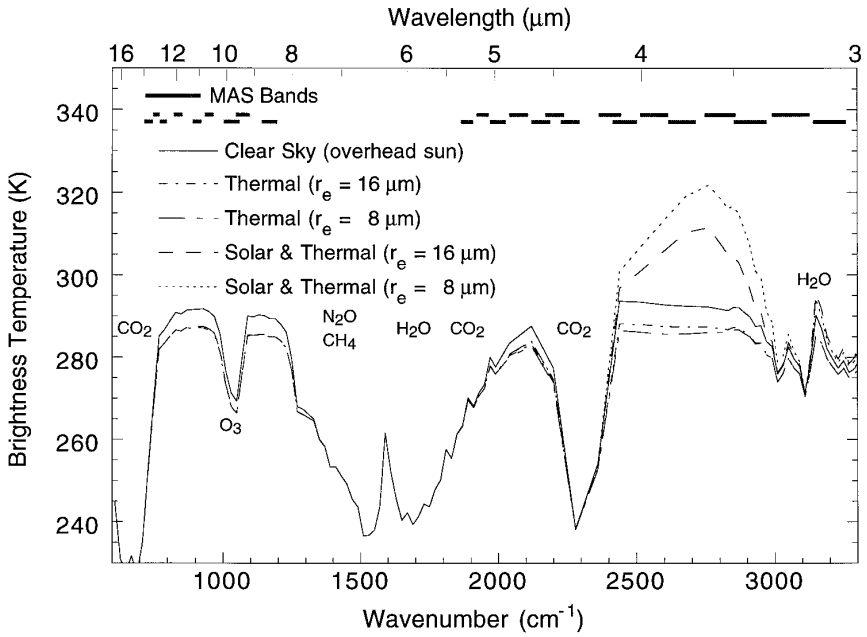

FIG. 2. Brightness temperature as a function of wavelength for nadir observations and for various values of the effective radius of cloud droplets, where the cloud optical thickness τ_c (0.75 μm) = 5 for all cases. Results apply to water clouds having a modified gamma distribution embedded in a midlatitude summer atmosphere with cloud-top temperature T_t = 14°C, cloud-base temperature T_b = 17°C, and an underlying surface temperature T_s = 21°C (assumed black). The location and bandwidth of MAS bands 27–50 are also shown in the figure.

both clear and cloudy sky conditions, where all computations were made using the discrete ordinates radiative transfer model developed by Tsay et al. (1990). These computations apply to midlatitude summer conditions, an oceanlike surface having a temperature of 294 K, unit emissivity (zero reflectance), and overhead sun. These computations further include gaseous absorption (water vapor, carbon dioxide, ozone, and the infrared water vapor continuum) at a 20-cm^{-1} spectral resolution (Tsay et al. 1989), with a low-level water cloud of optical thickness 5 (at 0.75 μm) placed at an altitude between 1 and 1.5 km.

In the 3.7-μm window, both solar reflected and thermal emitted radiation are significant, though the use of the reflectance for cloud droplet size retrieval is seen to be much more sensitive than the thermal component (note that, in either case, the thermal and solar signals must be separated to provide the desired component). CO_2 absorption is important around 4.3 μm and at wavelengths greater than about 13 μm; the MAS bands in these spectral regions can indicate vertical changes of temperature. The 4.82–5.28-μm channels are useful for investigating both horizontal and vertical distributions of moisture. Low-level moisture information is available in the split window measurements at 11.02 and 11.96 μm, and correction for moisture attenuation in the infrared windows at 3.90, 11.02, and 11.96 μm enables estimation of sea surface skin temperature (Smith et al. 1996).

The MAS infrared spectral bands enable the study of cloud properties at high spatial resolution. Products include cloud thermodynamic phase (ice vs water, clouds vs snow), cloud-top properties, and cloud fraction. The cloud-top properties (height, temperature, and effective emissivity) can be investigated using the CO_2 slicing algorithm (Wylie et al. 1994) that corrects for cloud semitransparency with the MAS infrared CO_2 bands at 11.02, 13.23, and 13.72 μm. Cloud phase can be obtained using MAS 8.60-, 11.02-, and 11.96-μm brightness temperature differencing (Strabala et al. 1994) as well as by using visible reflection function techniques (King et al. 1992) using ratios of the MAS 1.61- and 0.66-μm bands.

In addition to the remote sensing of cloud radiative and microphysical properties using reflected and emitted radiation, as illustrated in Figs. 1 and 2, the MAS is of great value for the remote sensing of land and water properties under clear sky conditions. MAS visible and near-infrared channels have been used to estimate suspended sediment concentration in nearshore waters and to identify water types (Moeller et al. 1993; Huh et al. 1996). Land vegetation properties can also be studied.

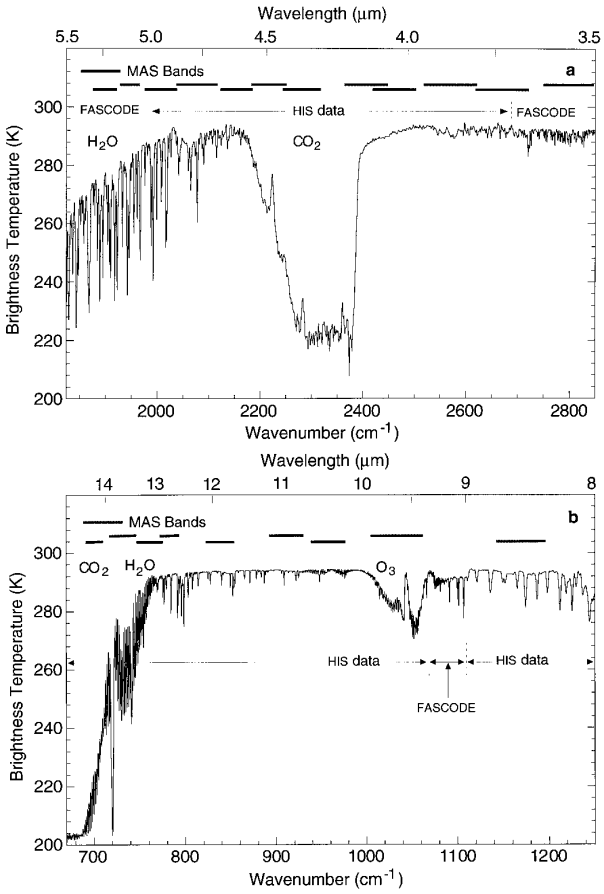

FIG. 3. HIS brightness temperature spectrum obtained between (a) 1850 and 2850 cm^{-1} (3.5 and 5.5 μm), and (b) 670 and 1250 cm^{-1} (8.0 and 14.9 μm) under clear sky conditions over the Gulf of Mexico (26°N, 93°40′W) on 16 January 1995. The location and bandwidth of MAS bands 30–50 are also shown in these figures. FASCOD3P computations were used to fill in missing sections of the infrared emission spectrum between 3.5 and 3.7, 5.0 and 5.5, and 9.0 and 9.3 μm.

Figures 3a,b illustrate emission spectra derived from High-resolution Interferometer Sounder (HIS) data (Revercomb et al. 1988) acquired from the ER-2 aircraft over the Gulf of Mexico (26°N, 93°40′W) on 16 January 1995. These data were obtained from an average of 27 clear-sky nadir views, where Fig. 3a applies to spectra between 1850 and 2850 cm^{-1} (3.5 and 5.5 μm), and Fig. 3b to spectra between 670 and 1250 cm^{-1} (8.0 and 14.9 μm). Superimposed on these figures are the location and bandwidth of MAS bands 30–50. Gaps in the HIS spectrum (between 3.5 and 3.7, 5.0 and 5.5, and 9.0 and 9.3 μm) are filled in with FASCOD3P (Clough et al. 1981) computations generated for clear sky conditions, a nadir view, and a temperature and humidity profile based on the U.S. standard atmosphere.

These measurements and computations, together with the bandpass characteristics of the MAS instrument, serve to illustrate the spectral richness in the infrared region due to absorption and emission by atmospheric carbon dioxide, water vapor, and ozone. Due to the large number of wavelengths not previously used experimentally from either aircraft or spacecraft sensors, the computations and measurements serve as an illustration of the information content, and relative strength, of the MAS channel placement in the thermal infrared region.

3. Instrument description

The MAS is a scanning spectrometer with 50 spectral bands in the wavelength range from 0.55 to 14.2 μm. Flown aboard a NASA ER-2 high-altitude research aircraft, the MAS is designed to scan through nadir in a plane perpendicular to the velocity vector of the aircraft (cross-track), with the maximum scan angle extending 42.96° on either side of nadir (85.92° full swath aperture). At a nominal ER-2 altitude of 20 km, this yields a swath width of 37.2 km centered on the aircraft ground track. A total of 716 earth-viewing pixels are acquired per scan at a scan rate of 6.25 Hz. Information provided by the aircraft inertial navigation system is used to adjust the timing of the digitizer, providing up to ±3.5° of roll compensation, in 0.03° increments. With each pixel having a 2.5-mrad (0.14°) instantaneous field of view, the spatial resolution at nadir is 50 m from the nominal aircraft altitude of 20 km. Table 1 summarizes the MAS specifications. A detailed description of the optical, mechanical, electronics, and data acquisition system design of the MAS follows.

TABLE 1. MODIS Airborne Simulator specifications.

Platform	NASA ER-2 aircraft
Altitude	20 km (nominal)
Ground speed	206 m s^{-1} (nominal)
Total field of view	85.92°
Swath width	37.25 km (at 20-km altitude)
Instantaneous field of view	2.5 mrad
Pixel spatial resolution	50 m (at 20-km altitude)
Pixels per scan line	716 (roll corrected)
Scan rate	6.25 scan lines per second
Spectral channels	50
Spectral range	0.55–14.2 μm
Data channels	12 (selected from 50 spectral channels) (1991–94) 50 (1995–)
Bits per channel	12 channels @ 8 bits (1991–94) 50 channels @ 12 bits (1995–); 16-bit dynamic range
Data rate	68.3 kbyte s^{-1} = 246 Mbyte h^{-1} (1991–94) 358 kbyte s^{-1} = 1.29 Gbyte h^{-1} (1995–)
Visible calibration	Integrating sphere on the ground
Infrared calibration	Two temperature controlled blackbodies on board

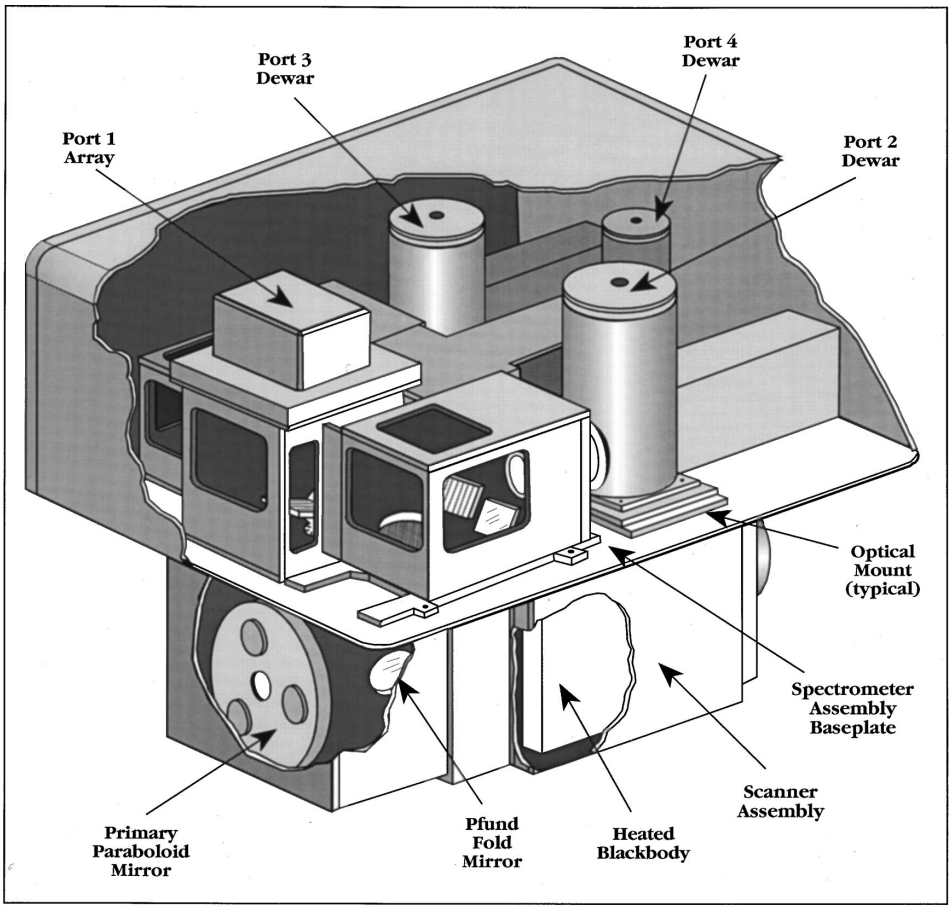

FIG. 4. Cutaway drawing of MAS. The spectrometer housing and scanner subassembly are approximately 59.7 cm long, 45.7 cm wide, and 48.2 cm deep, with the total system weighing 96 kg.

a. Optical design

The optical system of the MAS is composed of a complex configuration of dichroic beam splitters, collimating mirrors, folding mirrors, diffraction gratings, filters, lenses, and detector arrays. Figure 4 shows a cutaway drawing of the MAS, with the fore optics in the lower portion and the spectrometer modular assembly mounted above it. Both the spectrometer and fore optics portions are mounted to a 1.5-cm-thick aluminum optical baseplate assembly, which are pinned and mated. The fore optics consist of the constant rotation scan mirror, telescope, Pfund assembly (field stop and collimator), and onboard blackbodies. The upper portion contains the aft optics beam separating components, spectrometer ports, liquid nitrogen dewars, detector arrays, and detector electronics.

A full face scan mirror canted 45° to the along-track direction directs light into an afocal Gregorian telescope whose primary is a paraboloid mirror with a diameter and focal length of 15.2 cm, followed by a fold mirror that directs light back through a field stop aperture. A 2.5-cm Pfund assembly paraboloid forms a collimated image of the aperture, which strikes a fold mirror that directs the incoming radiation upward into the aft optics spectrometer unit. The aperture is located in the center of this fold mirror (cf. Fig. 5). Thermal and dark visible references are viewed on the backscan rotation of the scan mirror. The thermal reference sources are two blackened copper plate temperature-controllable blackbodies of a design previously proven on several different instruments (Jedlovec et al. 1989). One blackbody is viewed prior to the earth-viewing (active scan) portion of the scan, while the other is viewed following the active scan (cf. Fig. 6). Normally, the former is heated to around 30°C and the latter is either controlled down to −40°C, or allowed to float to ambient conditions (−20°C to −40°C). In addition, the blackened optical base provides a zero reference level when the instrument scans the vertical position. The telescope alignment is maintained under the extremely low temperature environment of the ER-2 using Invar steel and aluminum structural components.

As shown in Figs. 5 and 6, the collimated beam, having left the secondary telescope paraboloid mirror and fold mirror, passes vertically upward into the spectrometer through a hole in the baseplate, where it is wavelength separated by dichroic beam splitters and directed onto four focal plane assemblies (called ports). The spectrally broadband energy transmitted and reflected by the dichroics is dispersed onto the detector arrays from blazed diffraction gratings. The bandpass of a channel is determined by the geometry of the detector monolithic array and its location with respect to the grating. For the shortest wavelength port (port 1) and the shortwave infrared port (port 3), the grating approach optimizes the energy transmission and gives a sufficient signal-to-noise ratio. For the near-infrared channels (port 2) the detector sensitivity is considerably improved by employing a single broadband cold filter over the detector array to reduce background radiation. The port 4 channels also have the background noise further reduced by using a cold linear variable transmission filter mounted immediately in front of the detector array.

The radiation transmitted by the first dichroic D1 enters port 1, where it is reflected by a mirror and diffracted by grating G1 onto a filter and lens assembly that focuses the radiation onto a silicon photovoltaic array with channel response in the wavelength range from 0.55 to 0.95 μm (channels 1–9). Part of the radiation reflected by D1 reflects off the second dichroic D2 and enters port 2, where it is redirected by two fold mirrors, diffracted by grating G2, passed through a cold blocking filter, and focused onto an indium-antimonide (InSb) focal plane array assembly containing channels 10–25 ($1.61 \leqslant \lambda \leqslant 2.38$ μm). From D2, the remainder of the spectrally separated energy strikes the third dichroic D3, part of which is reflected and enters port 3, where it is redirected by two fold mirrors, diffracted by grating G3, and focused onto another InSb detector array that defines bandpass characteristics for channels 26–41 ($2.96 \leqslant \lambda \leqslant 5.28$ μm). The remainder of the energy from the scanner is transmitted through dichroic D3 into port 4, where it encounters a fold mirror, diffraction grating G4, and lens that focuses the thermal radiation onto three separate mercury–cadmium–telluride (HgCdTe) detector arrays, each with its own cold-filter to improve the signal-to-noise ratio in its respective wavelength range. Port 4 senses radiation in the wavelength range from 8.60 to 14.17 μm (channels 42–50). The InSb and HgCdTe detectors are cryogenically cooled by liquid nitrogen to 77 K in pressurized dewars, as illustrated in Figs. 4 and 6.

Table 2 shows the spectral and radiometric characteristics of each MAS channel in the complete 50-channel system. The spectral range of each spectrometer port is identified by a line break, and all 19 channels having close correspondence to MODIS spectral channels are indicated by the closest corresponding MODIS channel number. Spectral resolution, defined as the full-width at half-maximum bandwidth of the channel, ranges from around 40 nm in the visible and near-infrared to about 450 nm in the thermal infrared.

b. Mechanical design

The mechanical approach of the MAS was to assemble the instrument in two units, the scanner and the spectrometer. The scanner consists of a motor-driven rotating mirror and the blackbodies. The Speedring dc motor and angular position encoder are controlled by a closed loop proportional integrator, where the roll control is electrically timed to the scan window such that it has no effect on the constant speed scan mirror. The precision shaft is balanced and fitted with paired bearings to stabilize the cantilevered mirror.

The blackbodies are flat black painted copper plates about 6.3 mm thick and sized to overfill the clear aperture of the scanner assembly. Thermoelectric modules mounted on the back of the blackbodies are proportionally controlled and can raise or lower the temperature of the blackbodies from −40° to +40°C

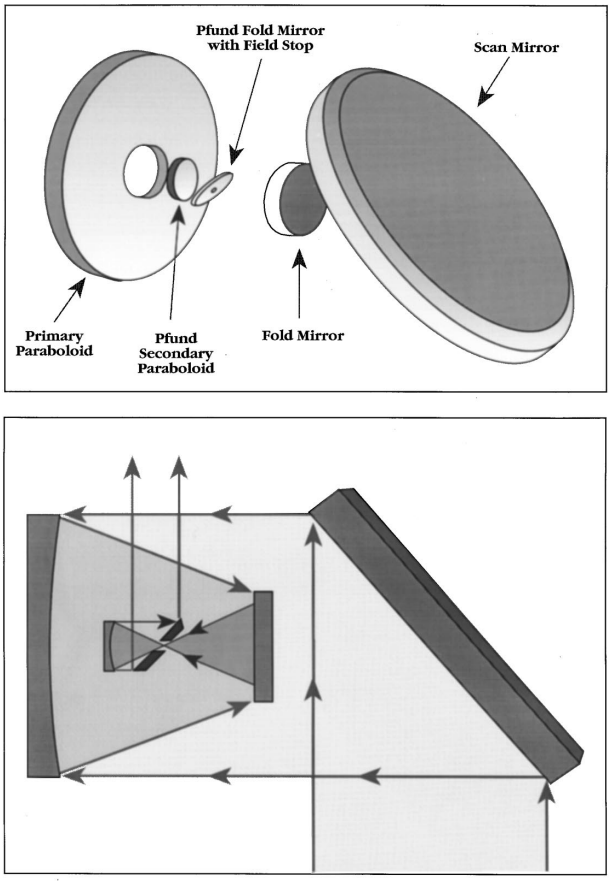

FIG. 5. Cutaway drawing of scanner subassembly, showing the scan mirror, primary mirror, fold mirror, and Pfund optics (secondary paraboloid, fold mirror, and field stop assembly).

(depending on dewpoint). Precision platinum resistance thermometers (PRTs) monitor the temperatures of the blackbodies, which are mounted to the scanner optical baseplate (cf. Fig. 4).

The scanner baseplate, to which the primary and secondary assemblies are mounted, as well as the surrounding scanner subassembly, consists of 1.5-cm-thick aluminum. Invar is used for critical assemblies with appropriate sliding fixtures to provide a temperature stable mounting platform.

The spectrometer unit is pinned and bolted to the scanner baseplate to preserve optical alignment integrity. Each detector port assembly is also pinned and secured to the spectrometer baseplate and mounted on a three-axis mount to allow the focal plane arrays to be precisely aligned. The spectrometer housing is enclosed by a 1-cm-thick insulating fiber blanket, to reduce the effects of the −20°C to −40°C (20-km altitude) operating environment on the spectrometer. Ten strategically placed Mylar film heaters beneath the insulation keep the instrument above the dewpoint at all times, preventing water damage to the spectrometer. The recently redesigned port 2 and 3 dewar assemblies resulted in a major decrease in the thermal deformations imposed on the dewar structures during flight conditions, resulting in a significant increase in the spectral stability of the instrument. Preamplifier circuits are included in the port 2 and 3 dewar packages, and preamplifiers for ports 1 and 4 are mounted in close proximity to the detectors. Some signal conditioning circuits are mounted in cases bolted to the spectrometer baseplate.

The overall size of the spectrometer housing and scanner subassembly is approximately 59.7 cm long, 45.7 cm wide and 48.2 cm deep, with the total system weighing approximately 96 kg. The MAS mounts in the rear unpressurized tailcone portion of the right wing superpod of the ER-2, where it scans through an open aperture roughly 23 cm along-track and 46 cm cross-track.

c. Electronics and data acquisition system

The data acquisition system (DAS) electronics are housed in the pressurized midbody section of the superpod on the forward side of a pressure bulkhead that is separated from the scanhead itself. The midbody is pressurized to 9-km equivalent altitude and maintained at a temperature of 0°C. The electronics components within the pressurized portion of the wingpod consist of a Dædalus AB325 motor and blackbody controller unit, the DAS (digitizer), and two 8-mm (Exabyte) tape recorders, all of which were designed to be insensitive to normal temperature variations encountered in the wingpod.

The AB325 controller drives the scan mirror motor, precisely controlling the rotation speed through a crystal frequency reference provided by the digitizer. It also actively maintains the temperature of the two blackbody thermal reference sources, which are preset before flight.

The digitizer unit, or DAS, is a state-of-the-art device designed by Berkeley Camera Engineering, using technology developed at the Space Sciences Laboratory of the University of California, Berkeley for infrared astronomy work. It is specifically optimized for low-noise digitization of analog signals produced by cryogenically cooled infrared detectors, where radiometric accuracy is of the utmost importance.

The signal train begins with the outputs of the 50 individual detector elements on the MAS, which pass through a set of low-noise preamplifiers on the scanhead, and are then fed through the pressure bulkhead via 50 sets of double-shielded, twisted-pair wires to the input of the digitizer. These analog inputs are each isolated electronically, and particular attention is paid to ground and power supply integrity to minimize noise.

A unique feature of the DAS is the set of preamplifiers that feed the analog-to-digital converters (ADCs). They are under active digital control to adapt to changing voltage levels from the scanhead, which compensates for the ''dc drift'' inherent in infrared detector systems. These drifts are the result of minute changes in the temperature of the liquid nitrogen in the dewars, together with subtle changes in the stability of the detector preamplifiers. This feature results in an extremely accurate quantization of the detector outputs, enabling a considerable improvement over traditional digitizer designs.

The conditioned analog signal is then passed to precision 16-bit ADCs for digitization. The 65 536 counts accommodate a range of radiances from the zero reference level to the saturation radiance in the shortwave channels and from the coldest to the warmest scenes in the thermal infrared. For surface viewing channels in the thermal infrared, the band saturation temperatures exceed 350 K, whereas for atmospheric viewing channels saturation temperatures generally exceed 300 K. Cross-track, the signal from the 2.5-mrad field of view is sampled every 0.5 mrad and lots of 5 are averaged to produce a scan line of contiguous 50-m pixels. Along-track, nominal aircraft speed (206 m s^{-1}) and mirror scan speed of 6.25 Hz indicate that the aircraft moves 33 m for every scan so that the 50-m pixels are oversampled by 34%. A series of digital signal processors (DSPs) perform the five sample cross-track averaging as well as correct for aircraft roll with information from the aircraft inertial navigation system (INS).

Other external data are also incorporated into the data stream at this time, including Global Positioning System (GPS) position and time code data, platform attitude from the INS, blackbody and scanhead temperatures, and exact scan motor speed from the AB325 controller. The data are then passed across a SCSI data bus, through a 486 processor chip, and onto the tape recorder unit.

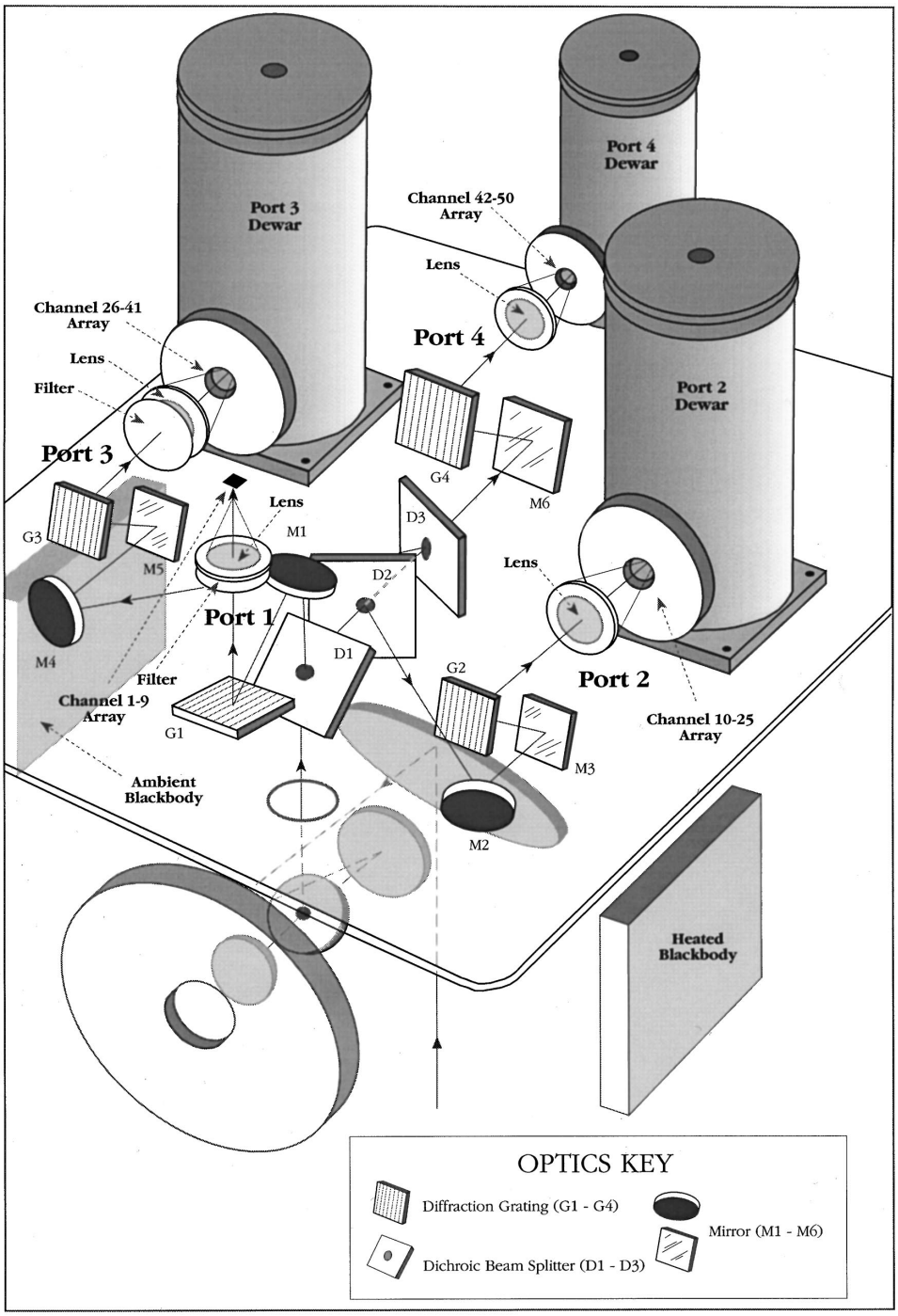

FIG. 6. Schematic diagram of the MAS optical system.

The recorder consists of two 5-Gbyte 8-mm tape drives that are shock-mounted in a nitrogen-purged, sealed housing. Together the two recorders can capture 7 h and 45 min of data. Because of bandwidth limitations on these recorders, only the high-order 12 bits of the original 16-bit values are stored, together with scaling factors. This enables the original 16-bit dynamic range of the data to be preserved in postprocessing. These tape drives will eventually be replaced by higher bandwidth hard disks or other tape devices.

TABLE 2. Spectral and radiometric characteristics of the 50-channel MODIS Airborne Simulator (MAS), including maximum radiance, noise equivalent radiance, noise equivalent temperature, ''typical'' scene brightness temperature, and signal-to-noise ratio. Ports 1–4 are delineated by blank lines and MAS channels having a close correspondence to MODIS channels are denoted by the closest corresponding MODIS channel number.

MAS channel	Equivalent MODIS channel	Central wavelength (μm)	Spectral resolution (μm)	Equivalent noise*	Scene temperature (K)**	Saturation level (W m^{-2} μm^{-1} sr^{-1})	Signal-to-noise ratio*
1	4	0.547	0.044	0.335		867	45.2–1052
2	1	0.657	0.053	0.157		1035	44.6–1948
3		0.704	0.042	0.178		1323	28.7–1586
4	15	0.745	0.041	0.180		1412	21.5–1406
5		0.786	0.041	0.254		1638	12.4–912
6		0.827	0.042	0.237		1890	10.7–923
7	2	0.869	0.042	0.281		1935	8.1–728
8	17	0.909	0.033	0.150		314	14.9–1232
9	19	0.947	0.046	0.226		1600	5.5–720
10	6	1.609	0.052	0.039		892	4.5–397
11		1.663	0.052	0.029		272	5.8–570
12		1.723	0.050	0.026		252	5.1–659
13		1.775	0.049	0.026		244	2.8–624
14		1.825	0.046	0.025		246	1.3–503
15		1.879	0.045	0.029		232	1.1–289
16		1.932	0.045	0.014		58	1.4–257
17		1.979	0.048	0.019		193	1.7–93
18		2.030	0.048	0.022		195	2.0–88
19		2.080	0.047	0.012		53	3.8–221
20	7	2.129	0.047	0.003		55	1.0–1309
21		2.178	0.047	0.023		211	2.3–255
22		2.227	0.047	0.026		240	2.0–245
23		2.276	0.046	0.027		263	1.6–198
24		2.327	0.047	0.026		268	1.5–140
25		2.375	0.047	0.033		329	1.0–83
26		2.96	0.16	9.78	291	TBD	1.7
27		3.11	0.16	7.05	284	TBD	2.4
28		3.28	0.16	3.09	284	TBD	5.9
29		3.42	0.17	1.28	291	TBD	15.7
30		3.59	0.16	0.72	293	TBD	29.7
31	20	3.74	0.15	0.47	293	TBD	47.5
32	21	3.90	0.17	0.37	292	TBD	62.4
33	23	4.05	0.16	0.30	289	TBD	78.2
34		4.21	0.16	0.81	257	TBD	23.8
35		4.36	0.15	1.74	234	TBD	9.5
36	25	4.52	0.16	0.28	272	TBD	83.2
37		4.67	0.16	0.14	289	TBD	192.9
38		4.82	0.16	0.13	286	TBD	210.2
39		4.97	0.15	0.12	286	TBD	234.9
40		5.12	0.16	0.14	280	TBD	199.7
41		5.28	0.16	0.18	275	TBD	153.7
42	29	8.60	0.44	0.14	292	TBD	363.2
43	30	9.79	0.62	0.12	287	TBD	465.0
44		10.55	0.49	0.09	294	TBD	697.7
45	31	11.02	0.54	0.10	294	TBD	654.7
46	32	11.96	0.45	0.19	294	TBD	370.9
47		12.88	0.46	0.46	291	TBD	161.2
48	33	13.23	0.47	0.49	283	TBD	147.0
49	35	13.72	0.60	1.32	256	TBD	46.7
50	36	14.17	0.42	2.00	229	TBD	25.5

* Noise equivalent ΔI (W m^{-2} μm^{-1} sr^{-1}) for channels 1–25; noise equivalent temperature difference NEΔT (K) for channels 26–50. All noise measurements are based on in-flight measurements over the Gulf of Mexico on 16 January 1995.

** The thermal data (channels 26–50) are based on in-flight measurements over the Gulf of Mexico on 16 January 1995 (clear-sky scene). The shortwave data (channels 1–25) are based on in-flight measurements over the Gulf of Mexico for the clear-sky scene (low signal level, where the reflectance is often less than 1%) and clouds on the north slope of Alaska on 7 June 1995 for the cloudy scene (high signal level). The range of signal-to-noise values for the shortwave channels reflects this range of scene radiance values.

4. Calibration

Radiometric calibration of the shortwave (<2.5 μm) channels is obtained by observing laboratory standard integrating sphere sources on the ground before and after flight missions, while calibration of the infrared channels is performed in flight by viewing two onboard blackbody sources once every scan. The blackbody sources are located on either side of the scan aperture in the scanner subassembly, as illustrated in Fig. 6.

a. Shortwave calibration

Two radiometric sources have been used for shortwave laboratory calibration during MAS development, a 30-in.-diameter (76.2 cm) integrating sphere maintained at Ames Research Center, and a 48-in.-diameter (121.9 cm) integrating hemisphere maintained at Goddard Space Flight Center. Both sources are coated with $BaSO_4$ paint and internally illuminated by 12 quartz-halogen lamps. The 30-in. sphere is used at Ames for MAS calibrations just prior to the ER-2 departure for field deployments as well as immediately following its return to Ames. This source is used to monitor long-term stability of the absolute calibration of the MAS. The 48-in. hemisphere has often been shipped to deployment sites and employed for MAS calibrations during the deployment. More recently, a 20-in.-diameter (50.8 cm) integrating hemisphere has been purchased by Ames to ship with the MAS on all deployments. The 20-in. integrating hemisphere is coated with Duraflect™ by Labsphere, North Sutton, New Hampshire, and is internally illuminated by 10 lamps. Recent intercomparisons with the 30-in. and 48-in. integrating sources suggest that this smaller more portable source is suitable for MAS field calibration purposes. This source is set up beneath the MAS prior to each ER-2 flight to monitor day-to-day fluctuations in the MAS shortwave calibration.

Calibration of the spherical integrating sources, both at Ames and during field deployments, is performed by Goddard personnel using a monochromator to transfer calibration to the integrating sources at spectral intervals of 10 nm. The monochromator consists of silicon, germanium, and lead sulfide detectors, each of which detects narrowband radiation dispersed from their individual gratings. The monochromator makes a relative measurement of input radiance with respect to a reference lamp in the wavelength range from 0.4 to 2.5 μm. The monochromator reference lamp is traceable to a standard lamp approved by the National Institute of Standards and Technology (NIST) and periodically checked against other instruments during round-robin intercomparisons.

The MAS shortwave calibration procedure involves viewing the spherical integrating sources through either a 20- or 25-cm opening on the side or top of the sources. Because of the MAS view angle position and physical constraints, calibrations using the larger 48-in. hemisphere require the use of a 45° inclined fold mirror that reflects the highly Lambertian radiation exiting the hemisphere upward into the MAS scanner. The smaller sphere and hemisphere can be viewed directly by the MAS scanner, since the exit opening is on the top of these sources and they are small enough to be positioned under the plane. The magnitude of the radiance incident on the spectrometer can be varied by changing the number of lamps illuminating the interior of the integrating source. The MAS is calibrated by measuring the digital output (counts) as a function of spectral radiance for varying illumination levels from the source. Taking a linear regression between digital counts and corresponding radiance levels permits the gain (radiance/count) to be determined for each channel, and allows the linearity of the instrument to be verified over the dynamic range of the expected signal levels. Thus, for each MAS shortwave channel, the radiance is related to digital count by

$$I_b = \frac{s_b(C_b - o_b)}{m_b},$$

where I_b is the radiance measured in each shortwave spectral band b, C_b is the count value representing the detector response to the integrating source, s_b is the slope, o_b is the offset (digital counts when observing ''zero'' radiance level), and m_b is the reflectance of the 45° mirror (not used since 1993).

MAS in-flight temperatures are typically below 0°C at ER-2 flight altitude, while calibrations are performed in the laboratory or aircraft hangar at much warmer temperatures. Without an in-flight shortwave calibration reference, changes in system performance during flight go undetected. However, the effect of environmental temperature on radiometric performance has been modeled from cold chamber measurements at Ames using the 20-in. integrating hemisphere as a stable source. Viewing this source in the thermal chamber, the sensor response at expected flight temperatures (as low as -35°C) is measured. Using these measurements, an algorithm describing shortwave radiometric performance as a function of instrument temperature is derived for each MAS channel. This algorithm, when used with actual measured flight temperatures (recorded by a separate recording system) is the ''temperature correction'' applied to MAS flight data to permit application of the laboratory-derived calibration.

The magnitude of the temperature correction has varied somewhat as the instrument has been modified. Port 1 channels show little temperature sensitivity in contrast to port 2 channels that have shown appreciable sensitivity. For example, thermal chamber tests for the Atlantic Stratocumulus Transition Experiment (ASTEX) calibrations, conducted in the Azores, Portugal, confirmed that port 1 gains

remained nearly constant with temperature, whereas port 2 gains decreased by up to 15% as the temperature was reduced to flight conditions. Installation of a new port 2 dewar in May 1994, just prior to the Monterey Area Ship Tracks (MAST) experiment, together with insulation and heating of the spectrometer head starting in December 1994, reduced the port 2 temperature sensitivity to a maximum of 8%. Cold chamber measurements, used for deriving postflight temperature corrections, are currently performed at atmospheric pressure, as opposed to the low-pressure environment encountered by the MAS while flying at ER-2 altitudes, though it is anticipated that a thermal vacuum test will be conducted in the near future. A summary of the shortwave calibration and temperature correction procedure is shown in Fig. 7; details are given by Arnold et al. (1994a,b).

Table 2 summarizes the single sample noise determinations for ports 1 and 2 from the 16 January 1995 flight over the Gulf of Mexico; a 100 pixel $\times$ 100 pixel box over a portion of the Gulf showing uniform radiance conditions was used in the noise determination. These data, together with mean values of the radiance for this low reflectance scene and a 300 pixel $\times$ 300 pixel bright cloud scene over the north slope of Alaska (discussed later in section 5) were used to determine the range of values for the spectral signal-to-noise ratio presented in Table 2. Given the noise levels presented in this table, one can easily compute the corresponding signal-to-noise ratio to be expected for any scene of interest.

b. Longwave calibration

The calibration of wavelengths greater than 2.96 μm is obtained from in-flight observations of two onboard blackbody sources, one operated at the ER-2 ambient temperature and the other at an elevated temperature (typically 30°C). The two blackbodies are coated with Krylon interior/exterior ultraflat black paint. The calibration slope and intercept for the thermal channels are determined from this two point measurement. The blackbody sources are viewed during every scan of the mirror (cf. Fig. 6).

The amount of energy received by the detector is related to the digitized count value by

$$I_b = s_b C_b + i_b,$$

where I_b is the radiance measured in each infrared spectral band b, C_b is the count value representing the detector voltage response to the scene radiance, s_b is the slope, and i_b is the intercept. We assume a linear response, as laboratory determinations indicate fractional nonlinearity parameters of less than 0.0001. The slope and intercept, and hence the calibration of counts to radiance, are calculated for each scan line using the count values recorded when viewing two onboard blackbody sources. Using w to indicate the warm blackbody, a to indicate the ambient blackbody, m to indicate the MAS instrument, and taking into account blackbody emissivity ϵ, then

$$s_b = \frac{\epsilon_b (I_{wb} - I_{ab})}{C_{wb} - C_{ab}},$$

$$i_b = I_{ab} + (I_m - I_{ab})(1 - \epsilon_b) - s_b C_{ab}.$$

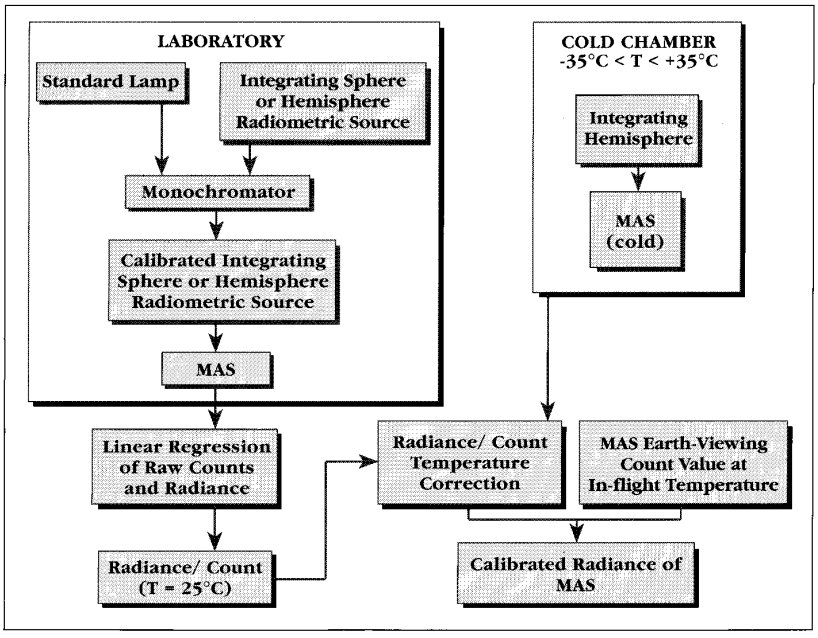

FIG. 7. Schematic representation of the MAS shortwave calibration procedure including radiometric source calibration and temperature correction.

TABLE 3. MAS infrared spectral band centers and corresponding adjusted Planck function coefficients.

MAS channel	Central wavelength (μm)	Central wavenumber (cm^{-1})	α_0	α_1
26	2.96	3381.81	0.86361	0.99906
27	3.11	3212.85	0.89794	0.99899
28	3.28	3048.78	0.74060	0.99913
29	3.42	2921.84	0.68543	0.99914
30	3.59	2785.90	0.56943	0.99925
31	3.74	2670.94	0.48670	0.99934
32	3.90	2562.46	0.45869	0.99935
33	4.05	2466.70	0.38325	0.99943
34	4.21	2376.99	0.36089	0.99945
35	4.36	2292.79	0.28303	0.99955
36	4.52	2214.10	0.27305	0.99956
37	4.67	2142.93	0.25647	0.99957
38	4.82	2073.40	0.22135	0.99962
39	4.97	2011.26	0.19684	0.99965
40	5.12	1951.41	0.18699	0.99966
41	5.28	1892.68	0.15156	0.99972
42	8.60	1162.25	0.30009	0.99915
43	9.79	1021.14	0.26925	0.99915
44	10.55	948.14	0.17352	0.99941
45	11.02	907.65	0.15770	0.99944
46	11.96	836.05	0.10462	0.99960
47	12.88	776.37	0.07082	0.99971
48	13.23	755.63	0.06844	0.99971
49	13.72	728.78	0.07238	0.99968
50	14.17	705.62	0.04547	0.99979

Blackbody count values are derived as the average of twelve FOVs across each blackbody surface during each scan, with the temperature of the blackbodies monitored by embedded thermistors. The emissivity of the blackbodies was obtained by viewing a well-characterized source in the laboratory, from which the emissivity was determined to be 0.94 and 0.98 for the longwave and shortwave infrared bands, respectively. For typical ocean scene temperatures, corrections for instrument radiation I_m reflected by the MAS blackbodies are approximately 1.25°C for the longwave and 0.25°C for the shortwave bands, respectively.

Equivalent Planck radiances from the blackbodies are calculated for each spectral band using a spectral response weighted integral of the form

$$I_b(T) = \frac{\int B(\lambda, T)F(\lambda)d\lambda}{\int F(\lambda)d\lambda},$$

where $B(\lambda, T)$ is the Planck function, $F(\lambda)$ is the spectral response for a given band, λ is wavelength, and T is the blackbody temperature. This can be fitted to an adjusted Planck function for the range of earth-emitted temperatures by introducing coefficients α_0 and α_1 such that

$$I_b(T) = B(\lambda_b, \alpha_1 T + \alpha_0),$$

where λ_b is the central wavelength or wavenumber of the band.

Table 3 indicates the fitted form of the Planck function for the infrared spectral bands on the MAS; the spectral band centers are indicated in wavelength (μm) as well as wavenumber (the number of wavelengths in one centimeter). The fitted form of the Planck function corrects for the nonmonochromatic nature of the measured radiation and is accurate to within 0.1°C for earth–atmosphere temperatures. Spectral response functions were measured at NASA Ames Research Center in August 1995 (see section 4c). Before compiling the data in Table 3, the spectral response measurements were filtered using a Savistky-Golay (Bromba and Ziegler 1981) averaging filter, truncated to remove unrealistic wing response and renormalized to remove offsets. Future hardware modifications may impact the data given in Table 3.

Calibration of the MAS infrared spectral bands has been validated in a field experiment where a NASA ER-2 with the MAS and HIS flew over a ship in the Gulf of Mexico taking measurements of the sea surface temperature, the upwelling infrared radiances, and the downwelling infrared radiances (Smith et al. 1996). After corrections for sea surface emissivity and reflections of atmospheric background radiation, we found that the HIS determinations of sea surface temperature were within 0.1°C of in situ measurements. Thus, the HIS spectral measurements offer a very good reference for the window spectral bands on the MAS. Table 4 shows the comparison of MAS and HIS radiance measurements integrated over the MAS spectral response functions; agreement is found to be within 1°C. The comparison was made using 527 collocations of MAS and HIS measurements over the deep-water Gulf of Mexico and includes the effect of nonunity emissivity of the blackbodies. MAS scan angle effects are minimal ($<$0.1°C) since only data within $\pm$3° of nadir are used.

Table 2 summarizes the single sample noise determinations for ports 3 and 4 from the 16 January 1995 flight over the Gulf of Mexico; a 100 pixel $\times$ 100 pixel box over a portion of the gulf showing uniform temperature and moisture conditions was used in the noise

TABLE 4. MAS window region surface temperature measurements in kelvins compared with HIS temperature measurements derived from HIS spectra integrated over the MAS spectral response functions.

MAS channel	Central wavelength (μm)	MAS-derived temperature (K)	HIS-derived temperature (K)	ΔT (K)
32	3.90	292.0	293.4	−1.4
42	8.60	291.3	292.2	−0.9
44	10.55	293.2	293.8	−0.6
45	11.02	293.3	293.9	−0.6
46	11.96	292.6	293.1	−0.5

determination. Single sample noise values are between 0.1° and 0.2°C for the spectral bands between 4.5 and 12.0 μm (roughly a factor of 4 improvement over previous versions of the MAS).

c. *Spectral characterization*

In August 1995 the spectral response characteristics of the MAS were measured at the Ames Research Center calibration facility. A highly monochromatic light source scanned the channel spectral bands. The interval was typically about 1.0% of the channel bandpass and scanning was initiated well short of the bandpass and ended well beyond the bandpass. All 50 channels were scanned to determine the structure of the bandpass envelope. The tests were performed on an optical bench using a 25-cm single-grating monochromator with a light source consisting of a 100-W tungsten halogen lamp and a 100-W Nernst glow bar. The light exiting the monochromator was collimated before entering the MAS instrument. Prior to these measurements, the wavelength accuracy of the monochromator was checked using a low pressure mercury standard discharge lamp and higher orders of a helium–neon laser. Absolute wavelength accuracy was determined to be about 0.2 and 2 nm in the visible and infrared regions, respectively. For all ports, the image of the monochromator slit was aligned with the spectral dispersion direction of the MAS spectrometer.

The signal flux to the instrument was low due to the narrow bandpass interval selected to examine spectral band structure. As a consequence, a lock-in amplifier and chopper were used to improve the signal-to-noise ratio as well as to reject spurious signals due to laboratory illumination and thermal conditions. The MAS output and calibrated reference detector signals were recorded at the grating monochromator step rate. Random noise in the calibrated reference detector data was reduced in post processing by fitting the reference data with a second-order function. Spectral absorption features were superimposed on the second-order function using FASCOD3P transmittances (at laboratory ambient conditions). The MAS output signal and noise-reduced reference signal were then ratioed to remove the effects of light source and monochromator signal spectral variation and beam path attenuation. These measurements form the basis of the central wavelength and spectral resolution (full width at half maximum) reported in Table 2.

5. In-flight performance

MAS image data are sampled at constant viewing angle intervals, which causes distortion of surface and cloud features near the edge of the swath. Pixels toward the edge of the scan include radiation from a larger area on the surface, as is the case with satellite cross-track scanners, since the cross-track pixel size at the surface is directly proportional to $\sec^2(\theta)$, where θ is the angle from nadir. At the nominal altitude and speed of the ER-2 aircraft, there is an oversampling of the pixels in the along-track direction by 34% at ground level.

Figure 8 shows a geometrically corrected false-color image and gray shade image of Atchafalaya Bay, Louisiana, acquired on 8 January 1995. The false-color image was constructed by contrast stretching and combining three different MAS spectral bands in one 24-bit image, where the spectral bands are assigned to red, green, and blue (RGB) 8-bit display channels. To obtain contrast between deep water, shallow shoals, and sediment from the river drainage into the Gulf of Mexico, the RGB assignment over the water was as follows: 0.704 μm (red), 0.657 μm (green), which shows suspended sediment, and 0.547 μm (blue), which shows reflectance from water surfaces. This combination of spectral bands emphasizes the contrast between shallow shoals (white region southwest of Point Au Fer Island in the lower right-hand portion of the image), deep gulf water (blue region just west of the shallow shoals) and sediment rich outflow waters (yellowish green). Over the land, 0.947 μm was used instead of 0.704 μm for the red assignment in order to emphasize vegetation, which is more highly reflective in this region. The gray shade image in Fig. 8 is an 11.02-μm thermal image that highlights the 2°–3°C temperature contrast between the cool river outflows and the shallow shoals of the nearshore Gulf of Mexico. Also apparent in this image is the cold core rings west of Point Au Fer Island.

Figure 8 illustrates that the high spatial resolution of MAS is useful for studying geomorphic evolution along the Louisiana coast. MAS visible and near-infrared channels can be used to track the response of nearshore suspended sediment to wind patterns of cold front passages (Moeller et al. 1993). Coastal circulation (by tracking features in time), land growth or loss, and sea surface temperature (SST) response can also be investigated using MAS visible and infrared channels.

Figure 9 shows high-resolution images of a convective cumulonimbus cloud surrounded by lower-level water clouds on the northern foothills of the Brooks Range, Alaska (69°7′N, 148°34′W), near the town of Sagwon, acquired on 7 June 1995. In contrast to Fig. 8, which was remapped to uniform spatial scale at the earth's surface, the panels in Fig. 9 are raw images consisting of 716 pixels cross-track and 716 scan lines along-track, and are oriented from south (at the top) to north (at the bottom), where the aircraft heading was 352°. The panel in the upper left (0.657 μm) shows high contrast between the optically thick (and therefore bright) cumulonimbus cloud, diffuse cirrus anvil, and remnants of the snow pack lying in ravines and topographic depressions (right center of image), less reflective altocumulus clouds (upper portion of image), and dark tundra. In contrast, the panel in the upper right (1.609 μm) shows that the cumulonimbus and cirrus

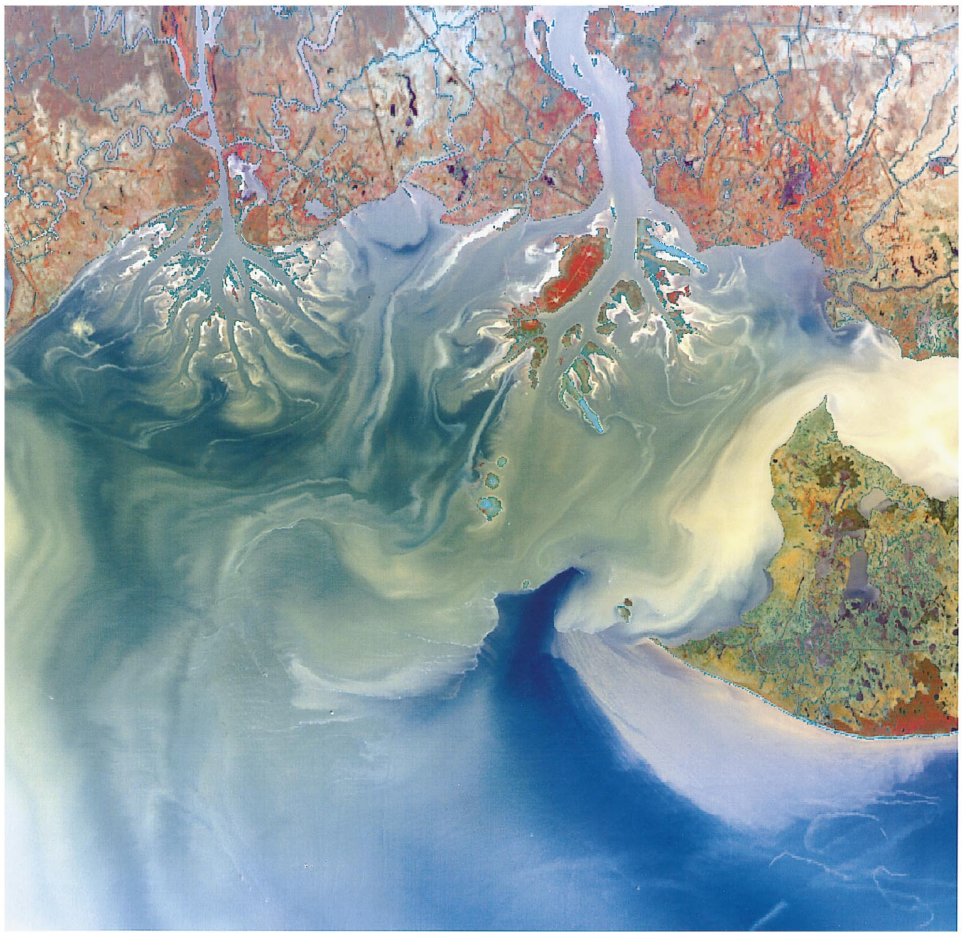

FIG. 8. Composite reflectance image and gray shade 11.02-μm thermal image (facing page) of Atchafalaya Bay, Louisiana obtained at 1630 UTC 8 January 1995. These images have been resampled to a constant 60-m resolution. The composite reflectance image over the water was constructed with the red assignment channel 3 (0.704 μm), the green assignment channel 2 (0.657 μm), and the blue assignment channel 1 (0.547 μm). To avoid saturation, the land areas used a red assignment of channel 9 (0.947 μm) rather than channel 3. The land mass at the right of the image is the west end of Point Au Fer Island, with the Lower Atchafalaya River and Wax Lake outflows on the top of each image. Turbid water from these outflows fills the Atchafalaya Bay region. Note also the 2°–3°C thermal contrast between the cool river outflows and the shallow shoals of the nearshore Gulf of Mexico.

anvil are composed of ice (low reflectance) and the surrounding altocumulus clouds are composed of water (high reflectance), as expected. The 1.879-μm panel in the lower left is especially sensitive to water vapor absorption in the atmosphere (cf. Fig. 1), and thus the high cumulonimbus and cirrus clouds are bright (little water vapor absorption above the cloud), whereas the lower-level altocumulus cloud and surface are darker due to absorption by water vapor in passing through a deeper column of the atmosphere (cf. Gao et al. 1993). To support this interpretation, the 11.02-μm panel in the lower right appears quite cold (low radiance) in the coldest portion of the cumulonimbus cloud (−50°C), warmer at the top of the altocumulus cloud (−18°C) where the cloud must be composed of supercooled water rather than ice (according to the 1.609-μm channel), and warmest at the surface (+17°C).

Images such as these serve to illustrate the extraordinary capability and quality of the data produced by MAS. The high quality, low noise, and wide swath width of this sensor make it an ideal instrument for a wide variety of atmosphere, ocean, and land applications.

6. Future plans

Based on initial operational experience, we currently anticipate a number of improvements, enhancements

FIG. 8. (*Continued*)

of capability, and laboratory tests. Instrument enhancements include (i) the addition of an onboard shortwave calibration source to enable stability of shortwave calibration to be monitored in-flight, (ii) the installation of a mechanical shutter to protect the optics during the descent phase of the aircraft, and (iii) the addition of a blue channel at 0.47 μm to enhance the scientific value of the MAS for ocean color and atmospheric aerosol applications. Laboratory measurements planned for the near future include (i) comprehensive thermal vacuum chamber testing and analysis to enable enhanced confidence in thermal correction algorithms, (ii) measuring and characterizing the polarization sensitivity of the MAS as a function of wavelength, (iii) measuring the modulation transfer function and point spread function of the MAS, (iv) viewing a calibrated high-temperature blackbody source, and (v) characterizing the spectral response functions periodically with high spectral resolution interferometric sources. Finally, we plan to improve the stability of the 20-in. integrating hemisphere that accompanies the MAS on field deployments by incorporating variable power supplies that are servo-controlled by reference detectors.

7. Conclusions

We have described the design and calibration of a spectrometer for making airborne measurements of the reflected and emitted radiation from the earth–atmosphere–ocean system. This instrument was developed as a multipurpose imaging spectrometer to obtain experimental measurements of the upwelling radiation field near the top of the atmosphere for the express purpose of testing algorithms for future satellite observing systems using real observations. The optical, mechanical, electrical, and data system design of MAS have been described, together with a description of protoflight and laboratory calibration checks. Finally, selected results from a cloud-free environment near the Louisiana coast, as well as a convective multilayer cloud system in the Alaskan arctic, have been presented to highlight the instrument performance.

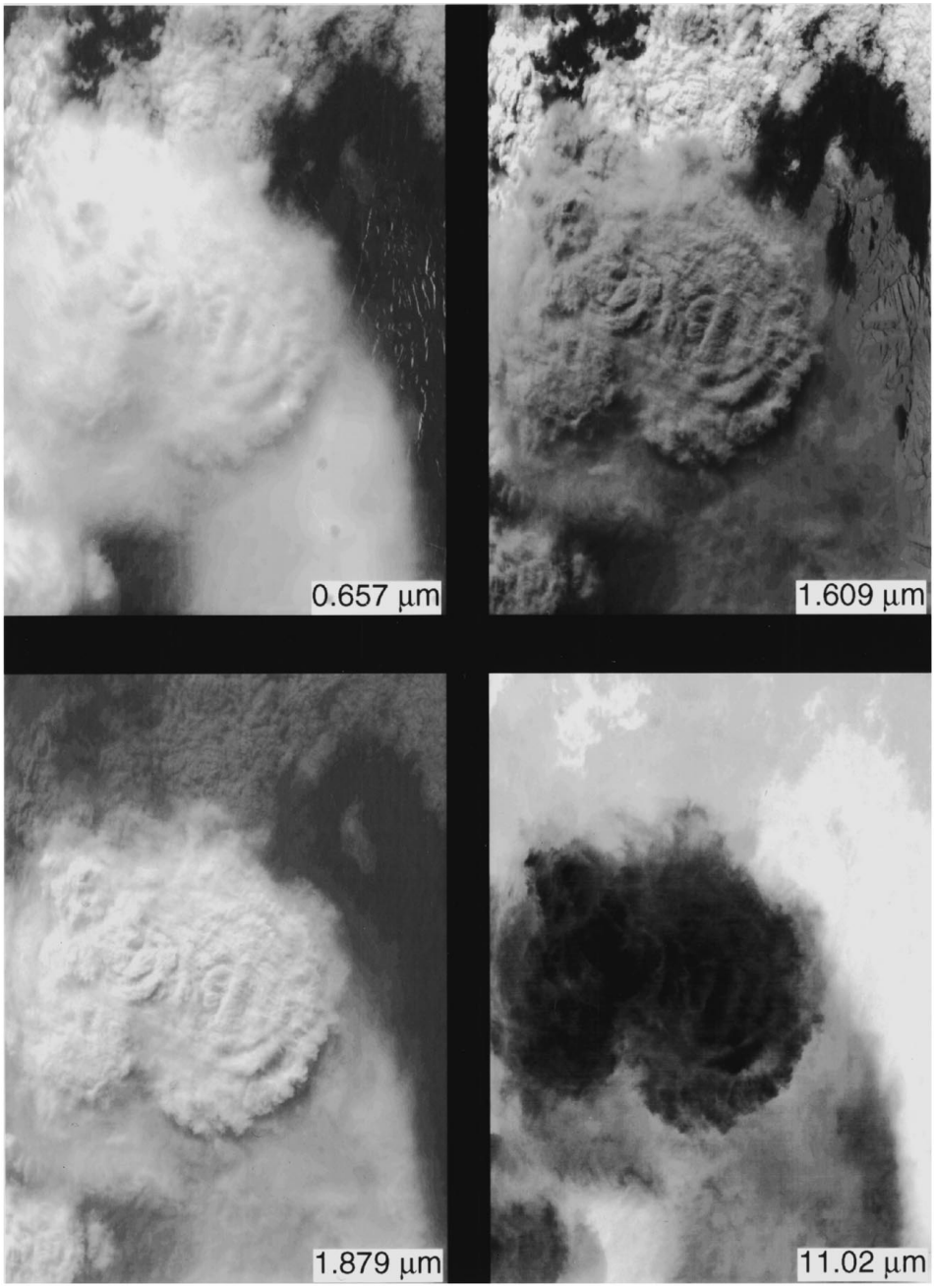

FIG. 9. MAS four-channel display of a convective cumulonimbus cloud surrounded by lower-level water clouds on the north slope of the Brooks Range (69°7′N, 148°34′W) on 7 June 1995. The image is a raw image consisting of 716 pixels cross-track and 716 scan lines along-track, and is oriented with the aircraft flight from south (top) to north (bottom). These panels show (from top left to lower right) imagery obtained from channel 2 (0.657 μm), channel 10 (1.609 μm), channel 15 (1.879 μm), and channel 45 (11.02 μm).

Of the 50 spectral channels of the MAS, 19 have corresponding channels on MODIS, a 36-channel spectroradiometer being developed for NASA's EOS AM-1 spacecraft, scheduled for launch in June 1998. These channels are specifically designed to enable the remote sensing of cloud optical thickness, effective radius, cloud-top properties (emissivity, pressure, temperature), water vapor column amount, and for determining a cloud mask (single layer, multilayer, clear sky, etc.). The physical principles behind the remote sensing of

atmospheric and land surface properties from MODIS can be found in King et al. (1992) and Running et al. (1994), respectively, as well as in algorithm theoretical basis documents available on the World Wide Web (http://eospso.gsfc.nasa.gov). In addition to these intended applications, many more uses can be found for the MAS, as demonstrated in Gumley and King (1995) for cloud-free observations of flooding in the Mississippi and Missouri River valleys during July 1993 and in Fig. 8 for estuarian outflows of river sediment into Atchafalaya Bay (Huh et al. 1996).

The MAS has thus far participated in field campaigns in the western tropical Pacific, the cerrado and rainforests of Brazil, the eastern subtropical Atlantic in the vicinity of the Azores, the east and west coasts of the United States, and the Alaskan high Arctic. In addition to numerous ER-2 deployments, the MAS has flown once aboard the NASA C-130B over boreal forests of Canada. A World Wide Web homepage has been established at http: / / ltpwww.gsfc.nasa.gov / MODIS / MAS / Home. html. From this point anyone with access to the Internet can retrieve a selection of 24-bit false-color MAS images, technical information and specifications of the MAS, reduced resolution ''browse'' images from all MAS flight lines during MAS field experiments, instructions on how to obtain, unpack, and interpret processed MAS data, and a printable and viewable copy of the MAS Level 1B Data User's Guide (Gumley et al. 1994). Processed MAS data are available through relevant EOS Distributed Active Archive Centers (DAACs). The specific point of data distribution is clearly identified as part of the browse imagery archive portion of this Web page. Any interested investigator can thereby obtain datasets for any flight or experiment that has thus far been processed. Scientific results from past and future experiments will be presented and analyzed in future contributions.

Acknowledgments. The authors are grateful for the many contributions of the High Altitude Missions Branch at NASA Ames Research Center and the Cloud Retrieval Group at NASA Goddard Space Flight Center. We are especially grateful to J. C. Arvesen for cooperation and support during integration and testing of the MODIS Airborne Simulator; G. J. Jedlovec and E. A. Hildum for developing the quick-look data visualization system for the earlier 12-channel data system; D. R. Smyrl, K. N. Dunwoody, and J. R. Bush for engineering support during various field deployments conducted throughout the world; R. Vogler for computer-aided design analysis; S. Spangler for computer graphics design; D. E. Wolf for rewriting the quick-look data visualization software for the 50-channel data system; M. C. Peck of Berkeley Camera Engineering for designing the 50-channel data system; and J. Green of Dædalus Enterprises for technical insights in enhancing the capabilities of the MAS. This research was supported by funding provided by the MODIS Science Team, the EOS Project Science Office, and NASA's Radiation Science Program.

REFERENCES

Ardanuy, P. E., D. Han, and V. V. Salomonson, 1991: The Moderate Resolution Imaging Spectrometer (MODIS) science and data system requirements. *IEEE Trans. Geosci. Remote Sens.,* **29,** 75–88.

Arnold, G. T., M. Fitzgerald, P. S. Grant, and M. D. King, 1994a: MODIS airborne simulator visible and near-infrared calibration—1992 ASTEX Field Experiment: Calibration version—ASTEX King 1.0. NASA Tech. Memo. 104599, Goddard Space Flight Center, Greenbelt, MD, 19 pp.

——, ——, ——, and ——, 1994b: MODIS airborne simulator visible and near-infrared calibration—1991 FIRE-Cirrus Field Experiment: Calibration version—FIRE King 1.1. NASA Tech. Memo. 104600, Goddard Space Flight Center, Greenbelt, MD, 23 pp.

Bromba, M. U. A., and H. Ziegler, 1981: Digital filter for computationally efficient smoothing of noisy spectra. *Anal. Chem.,* **53,** 1299–1302.

Clough, S. A., F. X. Kneizys, L. S. Rothman, and W. O. Gallery, 1981: Atmospheric spectral transmittance and radiance: FASCOD1B. *SPIE,* **277,** 152–166.

Gao, B. C., A. F. H. Goetz, and W. J. Wiscombe, 1993: Cirrus cloud detection from airborne imaging spectrometer data using the 1.38 μm water vapor band. *Geophys. Res. Lett.,* **20,** 301–304.

Gumley, L. E., and M. D. King, 1995: Remote sensing of flooding in the U.S. upper midwest during the summer of 1993. *Bull. Amer. Meteor. Soc.,* **76,** 933–943.

——, P. A. Hubanks, and E. J. Masuoka, 1994: MODIS airborne simulator level 1B data user's guide. NASA Tech. Memo. 104594, Vol. 3, Goddard Space Flight Center, Greenbelt, MD, 37 pp.

Huh, O. K., C. C. Moeller, W. P. Menzel, L. J. Rouse Jr., and H. H. Roberts, 1996: Remote sensing of turbid coastal and estuarine water: A method of multispectral water-type analysis. *J. Coastal Res.,* in press.

Jedlovec, G. J., K. B. Batson, R. J. Atkinson, C. C. Moeller, W. P. Menzel, and M. W. James, 1989: Improved capabilities of the Multispectral Atmospheric Mapping Sensor (MAMS). NASA Tech. Memo. 100352, Marshall Space Flight Center, Huntsville, AL, 71 pp.

Kaufman, Y. J., and B. C. Gao, 1992: Remote sensing of water vapor in the near IR from EOS/MODIS. *IEEE Trans. Geosci. Remote Sens.,* **30,** 871–884.

King, M. D., Y. J. Kaufman, W. P. Menzel, and D. Tanré, 1992: Remote sensing of cloud, aerosol, and water vapor properties from the Moderate Resolution Imaging Spectrometer (MODIS). *IEEE Trans. Geosci. Remote Sens.,* **30,** 2–27.

——, D. D. Herring, and D. J. Diner, 1995: The Earth Observing System (EOS): A space-based program for assessing mankind's impact on the global environment. *Opt. Photon. News,* **6,** 34–39.

Moeller, C. C., O. K. Huh, H. H. Roberts, L. E. Gumley, and W. P. Menzel, 1993: Response of Louisiana coastal environments to a cold front passage. *J. Coastal Res.,* **9,** 434–447.

Nakajima, T., and M. D. King, 1990: Determination of the optical thickness and effective particle radius of clouds from reflected solar radiation measurements. Part I: Theory. *J. Atmos. Sci.,* **47,** 1878–1893.

Revercomb, H. E., H. Buijs, H. B. Howell, D. D. LaPorte, W. L. Smith, and L. A. Sromovsky, 1988: Radiometric calibration of IR Fourier transform spectrometers: Solution to a problem with the High-spectral resolution Interferometer Sounder. *Appl. Opt.,* **27,** 3210–3218.

Running, S. W., C. O. Justice, V. Salomonson, D. Hall, J. Barker, Y. J. Kaufman, A. H. Strahler, A. R. Huete, J. P. Muller, V. Vanderbilt, Z. M. Wan, P. Teillet, and D. Carneggie,

1994: Terrestrial remote sensing science and algorithms planned for EOS/MODIS. *Int. J. Remote Sens.*, **15,** 3587–3620.

Smith, W. L., R. O. Knuteson, H. E. Revercomb, W. Feltz, H. B. Howell, W. P. Menzel, N. R. Nalli, O. Brown, J. Brown, P. Minnett, and W. McKeown, 1996: Observations of the infrared radiative properties of the ocean—Implications for the measurement of sea surface temperature via satellite remote sensing. *Bull. Amer. Meteor. Soc.*, **77,** 41–51.

Strabala, K. I., S. A. Ackerman, and W. P. Menzel, 1994: Cloud properties inferred from 8–12-μm data. *J. Appl. Meteor.*, **33,** 212–229.

Tsay, S. C., K. Stamnes, and K. Jayaweera, 1989: Radiative energy balance in the cloudy and hazy Arctic. *J. Atmos. Sci.*, **46,** 1002–1018.

——, ——, and ——, 1990: Radiative transfer in planetary atmospheres: Development and verification of a unified model. *J. Quant. Spectrosc. Radiat. Transfer*, **43,** 133–148.

Twomey, S., and T. Cocks, 1982: Spectral reflectance of clouds in the near-infrared: Comparison of measurements and calculations. *J. Meteor. Soc. Japan*, **60,** 583–592.

Wylie, D. P., W. P. Menzel, H. M. Woolf, and K. I. Strabala, 1994: Four years of global cirrus cloud statistics using HIRS. *J. Climate*, **7,** 1972–1986.